RSC Advances

PAPER

View Article Online
View Journal | View Issue

Cite this: *RSC Adv.*, 2021, **11**, 20701

The uptake mechanism of palladium ions into Prussian-blue nanoparticles in a nitric acid solution toward application for the recycling of precious metals from electronic and nuclear wastes

Jun Onoe, *[a] Shinta Watanabe,[ac] Hideki Masuda,†[b] Yusuke Inaba,[c] Miki Harigai[c] and Kenji Takeshita[c]

We have investigated the uptake mechanism of palladium (Pd: one of the most important elements in industry used as a catalyst) ions into Prussian-blue nanoparticles (PBNPs) in a nitric acid solution *via* high-resolution electron transmission microscopy, inductively coupled plasma atomic emission spectroscopy, powder X-ray diffraction, and ultraviolet-visible-near infrared spectroscopy in combination with first principles calculations. Comparison of the structural and electronic properties of PBNPs between before and after a 24 h sorption test reveals that the Pd^{2+} ions incorporated into PBNPs by the substitution of Fe^{2+} ions of the PB framework while maintaining the crystal structure, and the substitution efficiency is estimated to be 87% per PB unit cell. This implies that 0.30 g of Pd can be recovered by using 1 g of PB having the chemical formula $KFe^{III}[Fe^{II}(CN)_6]$. The present finding suggests that PB (or its analogues) can be applied to recycle noble and rare metals from electronic and nuclear wastes.

Received 7th March 2021
Accepted 25th May 2021

DOI: 10.1039/d1ra01794b

rsc.li/rsc-advances

1. Introduction

The recovery of rare metals from both electronic wastes (E-wastes) and nuclear wastes (N-wastes) is a key technology for sustainably maintaining and developing our society from the viewpoints of energy and environmental issues.

In the former case, the abundance of rare metals (ruthenium: Ru, rhodium: Rh, palladium: Pd, rhenium: Re, osmium: Os, iridium: Ir, platinum: Pt, and gold: Au) is 10^{-6} to 10^{-9} order lesser than that of rock-forming elements (sodium: Na, magnesium: Mg, aluminum: Al, silicon: Si, potassium: K, calcium: Ca, and iron: Fe).[1] Although they are not uniformly scattered over the world in nature, fortunately, we have already stored them in E-wastes. For example, the amount of Au contained in 1 t of a mobile phone is 300–400 g, which is 10–80 times higher than that found in 1 t of natural ores. Other elements also demonstrate a situation similar to Au. Consequently, the recovery of those elements from E-wastes is much more effective and efficient compared to their collections from the natural ore. However, conventional processes for recycling precious metals (so-called INCO method) require numerous operations (distillation, oxidation, reduction, precipitation and separation), which make the processes complicated and time-consuming. In addition, it is hard to extract or adsorb trivalent metals (Ru, Ir, and Rh) chloride anions.

In the latter case, the spent nuclear fuels generated from the power plants are vitrified at the reprocessing plant. After the separation of uranium (U) and plutonium (Pu) from the spent fuels for reuse as new fuels using the PUREX (Plutonium Uranium Redox Extraction) method, the high-level radioactive liquid wastes (HLLWs) are vitrified and geologically disposed.[2–4] In the vitrification processes, the platinum-group metals (PGMs) (particularly Ru, Rh, and Pd) and molybdenum (Mo) cause severe problems: (i) PGMs tend to settle on the sidewall surface of a glass melter, resulting in an inhomogeneous thermal distribution of the melter, and (ii) Mo forms a low-viscosity fluid compound so-called "yellow phase" in the vitrified object.[5,6] These degrade the quality and stability of the vitrified objects due to heterogeneity and increase both the disposal spaces and cost in conjunction with additional vitrified rods obtained by flushing the glass melter. Considering that Ru, Rh, and Pd with amounts of 2.09, 0.36, and 1.20 kg, respectively, are generated in 1 t of used nuclear fuels (burnup: 30 000 MWd/t, cooling period: 150 days) for light-water reactors (their generated amounts will increase 1.5–2 times for fast breeder

[a]*Department of Energy Science and Engineering, Nagoya University, Furo-cho, Chikusa-ku, Nagoya, Aichi 464-8603, Japan. E-mail: j-onoe@energy.nagoya-u.ac.ne.jp; Fax: +81-52-789-3785; Tel: +81-52-789-3785*

[b]*Research Center for Advanced Measurement and Characterization, National Institute for Materials Science, 1-2-1 Sengen, Tsukuba, Ibaraki 305-0047, Japan*

[c]*Laboratory for Advanced Nuclear Energy, Tokyo Institute of Technology, 2-12-1-N1-16 Ookayama, Meguro-ku, Tokyo 152-8550, Japan*

† Present address: Advanced and Fundamental Technology Center, JEOL Ltd., 3-1-2 Musashino, Akishima, Tokyo 196-8558, Japan.

reactors), it is useful to recover PGMs from HLLW not only for the disposal of nuclear wastes but also for the recycling of rare metals from our alternative perspective. It is worth noting that it takes a few decades to reduce their radioactive levels below the safety standard except for ^{107}Pd long-lifetime nuclide (half-life: 6.5 million years). Recently, we have demonstrated that aluminum hexacyanoferrate, which is one of Prussian blue (PB) analogues, exhibits high uptake ability against PGMs in the nitric acid solution.[7] However, the uptake mechanism is still not clear, though it is important to develop higher performance sorbents.

The aim of the present study is to solve those issues using PB or PB analogues (PBAs), one of the metal hexacyanoferrates (MHCFs), as a sorbent.[8,9] Since MHCFs have a simple cubic lattice structure such as a jungle gym (Fig. 1), wherein divalent (M^{2+}) and trivalent (M^{3+}) metal cations are cross-linked with each other *via* a cyano-group anion (CN^-) and exhibit numerous fascinating features,[10–12] they have been extensively investigated from the viewpoints of both scientific and industrial aspects.[13–19] Recently, PB (FeHCF) was applied for the removal of radioactive cesium-134 (^{134}Cs) and ^{137}Cs from contaminated soils, which was caused by the Fukushima nuclear plant accident in 2011 (ref. 20–24) because PB has the jungle-gym cubic structure (see Fig. 1) with a 0.5 nm interstitial site (4c site in the $F\bar{4}3m$ space group) that played a role in trapping the Cs ions efficiently. The uptake mechanism of PB for multi-valent metal ions is still not clear, although three possible sorption processes can be considered: (i) surface adsorption, (ii) insertion or diffusion into the interstitial sites (nanospace) in a manner similar to Cs ions, and (iii) substitution of Fe with metals in the framework of PBs.

In order to develop high-performance MHCF sorbents for the recovery of PGMs from E- and N-wastes, it is necessary to reveal the sorption characteristics of PB for these metal ions. In the present study, we reported the uptake mechanism of Pd ions (as one of the representative of the rare metals) for PB nanoparticles (PBNPs) in nitric acid solution at the first stage. After the crystal structure and size distribution of pristine PBNPs were characterized *via* high-resolution transmission electron microscopy (HRTEM), the sorption efficiency of Ru, Rh, and Pd into PBNPs and the elution efficiency of Fe from PBNPs were examined by the 24 h sorption test using inductively coupled plasma atomic emission spectroscopy (ICP-AES). As shown in Table 1, since Pd exhibits the highest sorption efficiency among them, the uptake mechanism of Pd into PBNPs is focused in the present study. The changes in the structural and electronic properties of PBNPs before and after the sorption test of Pd ions *via* powder X-ray diffraction (XRD) and ultraviolet-visible-near IR (UV-Vis-NIR) spectroscopy techniques in combination with first principles calculations.

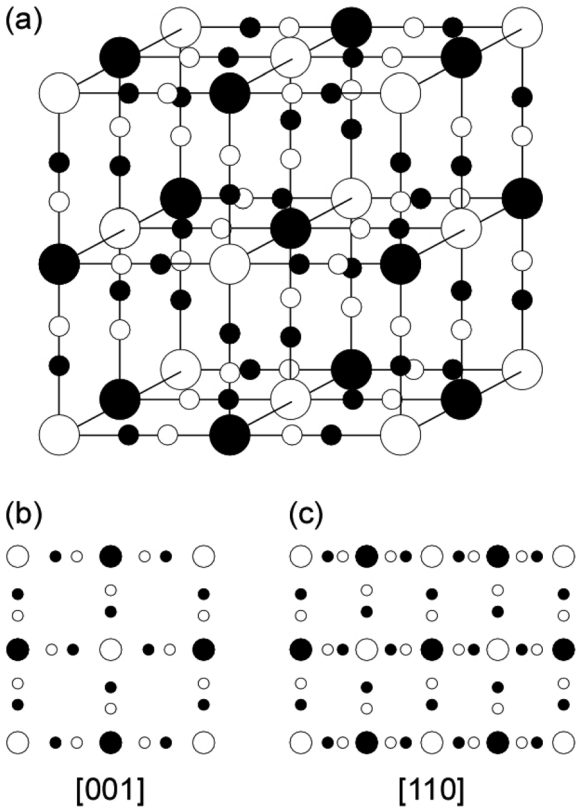

Fig. 1 (a) Schematic model of the unit cell for the cubic lattice structure of metallic ferrocyanide; (b) and (c) are the projected atomistic models along [001] and [110] directions, respectively.

2. Experimental and theoretical procedures

2.1. Experimental procedures

PBNPs were synthesized by mixing potassium hexacyanoferrate(II) (5 mmol, $K_4[Fe(CN)_6]\cdot 3H_2O$, Kanto Chemical) with iron(III) nitrate (10 mmol, $Fe(NO_3)\cdot 9H_2O$, Wako) in an aqueous solution. PB precipitates thus formed were rinsed with ultrapure water after centrifugation (3000 rpm) and filtration for five times. Subsequently, PBNPs were dried at 75 °C for 12 h and thereafter placed in the vacuum desiccator for 3 h.

The crystal structure and size distribution of PBNPs thus formed were examined *via* HRTEM (JEOL: JEM-2010F, an incident electron energy: 200 keV). A small amount (~0.01 mg) of the PBNP was introduced into a glass tube (15 mm in diameter and 40 mm in length). 10 mL of ethanol was added into the tube, and subsequently, NPs in ethanol were dispersed using an ultrasonic bath for 5 min. Thereafter, 10 μL of the supernatant solution was taken by a micropipette and dropped on a copper

Table 1 The sorption efficiency of Pd ions into PBNPs and the elution efficiency of Fe ions from PBNPs after the 24 h sorption test, along with those for Ru and Rh ions[a,b]

	Ru	Rh	Pd
Sorption efficiency (%)	33.1	68.2	99.9
Elution efficiency of Fe ion (%)	19.5	23.9	43.5
Substitution efficiency (%)	39.0*	47.8*	87.0
Amount of recovery per 1 g PB (g)	0.287*	0.292*	0.302

[a] *Prediction. [b] Sorption efficiency (%) = $(C_{initial} - C_{final})/C_{initial} \times 100$. Here, $C_{initial}$ and C_{final} denote the concentration of Pd ions in the nitric acid solution before and after the 24 h sorption test, respectively.

(Cu) mesh equipped with collodion carbon films. After the Cu mesh was dried in air for more than 30 min, PBNPs dispersed on the mesh were observed *via* HRTEM.

The sorption test of Pd ions (1 mM) for PBNPs (500 mg) was carried out in a 1.5 M nitric acid solution (10 mL) upon shaking for 24 h. Subsequently, the mixtures were centrifuged to separate the NPs from the solution, and the concentration (C) of Pd ions in the supernatant liquid was measured before (C_{initial}) and after (C_{final}) the test *via* ICP-AES (ICPE-9000, Shimadzu) in order to estimate the sorption efficiency $[(C_{\mathrm{initial}} - C_{\mathrm{final}})/C_{\mathrm{initial}} \times 100\%]$ of Pd ions into PBNPs. The concentration of Fe ion in the supernatant liquid after the sorption test was measured *via* ICP-AES, and the elution efficiency of Fe ions when compared to the initial amount of PBNPs was estimated. Details of the sorption test conditions were provided elsewhere.[7]

Powder XRD patterns and UV-Vis-NIR diffuse reflectance spectra of the pristine and Pd-sorbed PBNPs were measured using a Rigaku RINT2200 (Cu Kα) and Shimadzu UV-2600 spectrophotometer, respectively. The diffuse reflectance spectra thus obtained were converted to the corresponding absorption spectra in terms of the Kubelka–Munk conversion equation.

2.2. Theoretical calculations

The theoretical density-of-states (DOSs) and absorption spectra of pristine and Pd-sorbed PBs were examined using CASTEP,[25] which is one of the first principles calculations based on density functional theory (DFT).[26,27] The Vanderbilt form ultrasoft pseudopotentials[28] were adopted throughout the present calculations. The exchange–correlation potential was considered within GGA (PBE).[29] The cut-off energy for the plane wave is 550 eV, and the Brillouin zone was sampled on the 5 × 5 × 5 Monkhorst–Pack grid[30] for all of the primitive cell calculations. All of the DFT calculations were performed with the GGA+U method based on a simplified, rotationally invariant approach.[31] The numerical error was estimated to be less than 1 meV per atom by cut-off and k-point convergence tests. The geometric optimization was performed until the residual forces and stresses dropped below 0.01 eV Å^{-1} and 0.02 GPa, respectively.

3. Results and discussion

3.1. TEM characterization of PBNPs

Fig. 2(a) and (b) show a typical TEM image (inset shows the electron diffraction, ED, pattern) and the size distribution of the PBNP aggregates, respectively. Here, the surrounding gray image shows the carbon collodion film. The TEM images demonstrate that the PB formed an aggregate of NPs. The size of the aggregation is in an order of 100 nm, whereas the size of the PB primary NP is in the range of 6–26 nm with an average diameter of 13 nm (obtained from the result of Fig. 2(b)). As shown in the inset, the ED pattern shows a hallo pattern as the number of the PB aggregates on the carbon film is so less in the present observation. Thus, most part of the ED measurement area was the collodion film (amorphous carbon).[32] In order to examine the structure of the individual PBNP in detail, we next observed one of the primary PBNPs *via* HRTEM.

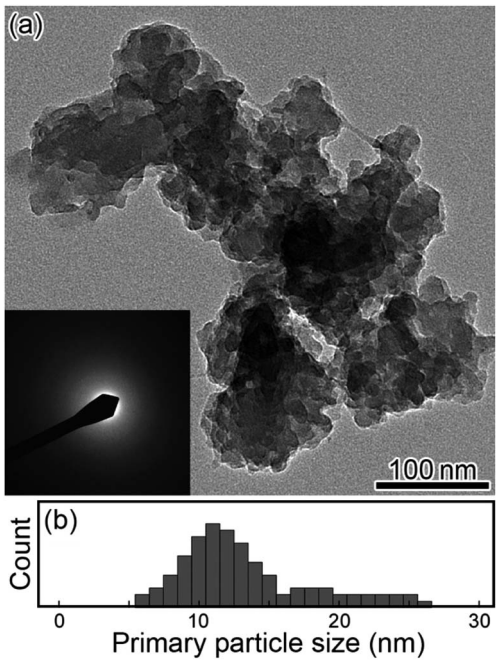

Fig. 2 (a) TEM image of PBNPs (inset: ED pattern) and (b) histogram of primary NP size.

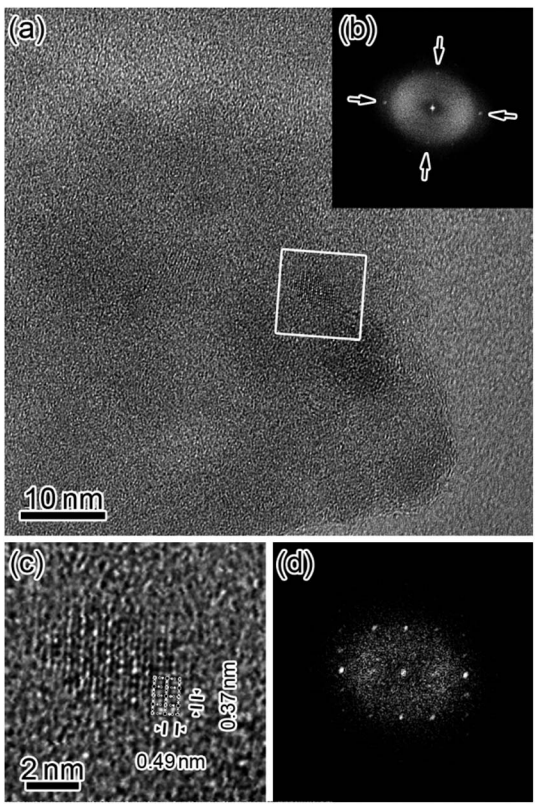

Fig. 3 (a) HRTEM image of PBNPs, (b) the FFT pattern corresponding to the HRTEM image, (c) the magnified HRTEM image focused on the PB crystalline NP, and (d) the FFT pattern corresponding to the magnified image.

Fig. 3 shows the HRTEM images of PBNPs at wide (a) and narrow (c) scales, along with their corresponding fast Fourier-transformed (FFT) patterns (b) and (d), respectively. Here, the white rectangle in the image (a) indicates the magnified area corresponding to image (c). As shown in Fig. 3(b), four orthogonal lattice fringes appear as indicated by arrows, and in fact, the FFT pattern (b) shows the spots corresponding to the lattice fringes. From the magnified image (c), we observed two different lattice distances of 0.49 nm and 0.37 nm, which are in good agreement with those of d_{002} (0.50 nm) and d_{220} (0.35 nm) for cubic lattice ($a = 1.00$ nm) of PB,[33] respectively. Accordingly, the HRTEM lattice image (c) seems to project the crystal structure of one PBNP itself. In order to confirm that the lattice image shows a simple cubic crystal structure, we next compared the magnified lattice image with a simulated one.

Fig. 4 shows the observed (a) and simulated (b) HR lattice images of the PB crystalline NP along the [110] direction. The former image (a) is taken from some small area in Fig. 3(c), whereas the latter image (b) is obtained using the QSTEM code[34] based on a multi-slice method. Comparison between them indicates that these are basically similar to each other, although the observed image (a) includes some electron-beam (EB) induced damages (some inhomogeneous contrasts) to some extent. Thus, the present TEM results demonstrated that PBNP possesses a simple cubic crystal structure (see Fig. 1).

3.2. Uptake mechanisms of Pd ions into PBNPs

Table 1 summarizes the sorption efficiency of Pd ions incorporated into PBNPs, the elution efficiency of Fe ions from PBNPs, the substitution efficiency of Pd with Fe, and the amount of Pd recovered per 1 g PB after the 24 h sorption test along with those for Ru and Rh ions. As shown in Table 1, Pd ions exhibited the highest sorption and elution efficiency values among the PGM ions. Thus, we focused on Pd ions in order to understand the sorption properties of PBNPs at the first stage. The other two terms (substitution efficiency and amount of uptake) will be discussed later.

Fig. 5 shows the UV-Vis-NIR spectra of PBNPs before (black) and after (red) Pd ion sorption. Here, the three arrows indicate

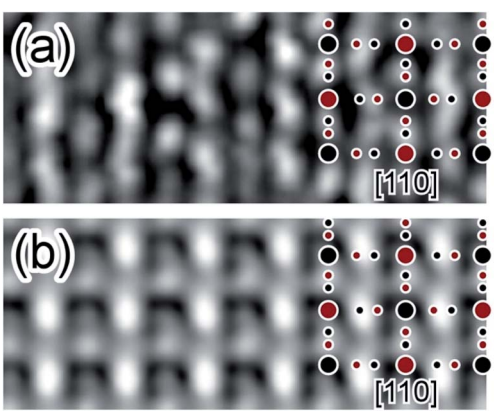

Fig. 4 Comparison between the observed (a) and simulated (b) HRTEM lattice images of the crystalline PBNP observed along the [110] direction.

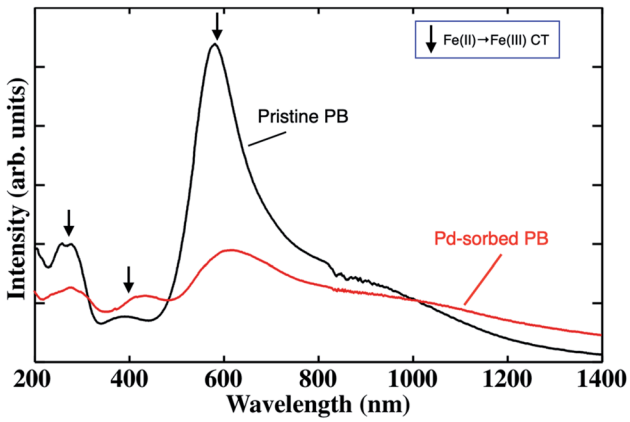

Fig. 5 UV-Vis-NIR spectra of PBNPs before (black) and after (red) Pd sorption. The arrows indicate the individual peaks originating from the Fe(II)–Fe(III) charge-transfer transitions. These spectra were not normalized at 215 nm.

the individual peaks originating from the charge-transfer (CT) transitions from Fe^{2+} to Fe^{3+}.[35] It can be seen that the two kinds of spectral changes after the sorption of the Pd ion: (i) a drastic decrease in the CT absorption intensity of around 600 nm and (ii) a new broad band appearing in the region of 1000–1400 nm and longer. Since the intense peak due to the Fe^{2+}–Fe^{3+} CT transitions around 600 nm drastically decreased after Pd sorption, it is reasonable to consider that Fe^{2+}/Fe^{3+} ions are substituted with Pd^{2+}. This is also strongly supported by the elution rate of Fe ion from PBNPs, as shown in Table 1.

To understand those spectral changes, we theoretically examined the electronic structure and absorption spectra for the pristine and Pd-sorbed PBNPs using two kinds of models: Pd^{2+} substituted with Fe^{2+} (Model 1) and with Fe^{3+} (Model 2). Fig. 6 shows the schematic illustration of two substitution models: Models 1 (left) and 2 (right) [top], theoretical density-of-states (DOSs) for Model 1 (left) and Model 2 (right) [middle], and theoretical absorption spectra for Model 1 (left: red) and Model 2 (right: green) along with that of the pristine PB (blue) [bottom]. For the results of DOS, the Fermi level (E_F) is located at 0 eV, the occupied and unoccupied DOSs are located below and above E_F, respectively, and the positive and negative values of DOS indicate the up and down spin states, respectively. The partial DOSs shown by gray, blue, and red colors correspond to the s-, p-, and d-orbitals, respectively. As shown in Fig. 6, Model 1 (Fe^{2+} → Pd^{2+} substitution) indicates that the valence band at E_F and below consists of the Pd^{2+}-4d orbital, whereas the lowest unoccupied band consists of the Fe^{3+}-3d orbital. On the other hand, Model 2 (Fe^{3+} → Pd^{2+} substitution) indicates that the valence band at E_F and below consists of the Fe^{2+}-3d orbital, whereas the lowest unoccupied band consists of the Pd^{2+}-4d orbital. The difference in the energy levels between the Pd^{2+}-4d and Fe^{3+}-3d DOSs for Model 1 became smaller when compared to that obtained between the Fe^{2+}-3d and Fe^{3+}-3d DOSs for the pristine PB (see Fig. 3 of ref. 35), whereas the energy difference between the Fe^{2+}-3d and Pd^{2+}-4d DOSs for Model 2 became larger than that obtained between the Fe^{2+}-3d and Fe^{3+}-3d DOSs for the pristine PB. Correspondingly, the absorption band due to CT transitions is red-

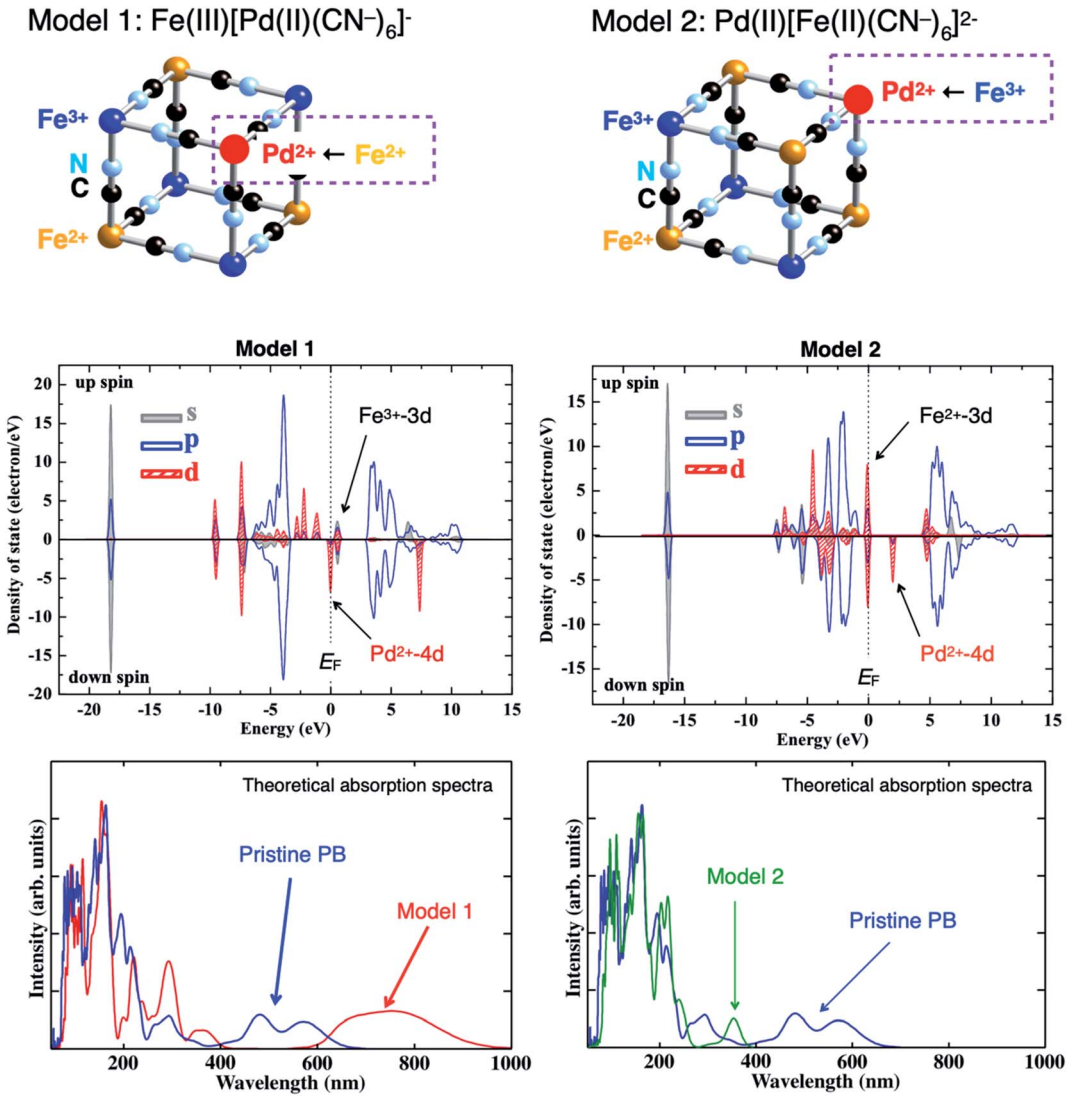

Fig. 6 Schematic of two substitution models (top). Theoretical density-of-states (DOS) for Model 1 (left) and Model 2 (right) (middle). Here, the Fermi level (E_F) is located at 0 eV along the energy axis. The occupied and unoccupied DOSs are located below and above E_F, respectively. The positive and negative values of DOS indicate the up and down spin states, respectively. The partial DOSs indicated by gray, blue, and red denote s-, p-, and d-orbitals, respectively. Theoretical absorption spectra of Model 1 (left: red) and Model 2 (right: green) along with that of pristine PB (blue) (bottom).

and blue-shifted for Model 1 and Model 2, respectively, when compared to that obtained before Pd sorption [bottom]. Consequently, Model 1 qualitatively explained the spectral changes of PBNPs after Pd sorption (Fig. 5), thus concluding that Pd^{2+} ion was substituted with Fe^{2+} ion of PB.

Since the ionic radius (0.78 Å) of Pd^{2+} is a little larger than that (0.75 Å) of Fe^{2+},[36] the lattice constant should be expanded to some extent after the substitution of Pd^{2+} with Fe^{2+} completely. Then, we measured the XRD patterns of PBNPs before (black) and after (red) Pd-ion sorption. As shown in Fig. 7, the XRD pattern (black) shows that PBNP has a face centered cubic (FCC) structure (space group: $F\bar{4}3m$), which is consistent with the TEM results of Fig. 3 and 4. The lattice constant and crystallite size were estimated by fitting the (200) diffraction peak with the pseudo-Voigt function and using the Scherrer equation[37] with a constant of 1.5, respectively. Here, the constant value meant an area-weighted effective diameter along the direction of the diffraction vector. Since PB has the FCC structure and its XRD pattern was fitted with the (200) plane diffraction peak, the crystallite size was found to be 16 nm using the Scherrer equation, which is a little bit larger than that (13 nm) obtained from TEM results of Fig. 2. The TEM technique measured the supernatant of the ultrasonically dispersed fraction of PBNPs, which contained smaller NPs in the ensemble, while the larger ones remained not solubilized in ethanol when the TEM samples were prepared. Thus, the average size of the entire ensemble measured *via* XRD is larger than that obtained by TEM.

In addition, it was obtained from both XRD patterns that the lattice constant was estimated to be 10.16 Å for the pristine PBNPs and 10.21 Å for the Pd-sorbed PBNPs. This indicated that the lattice constant was effectively expanded after Pd ion substitution. Furthermore, since the two XRD patterns were

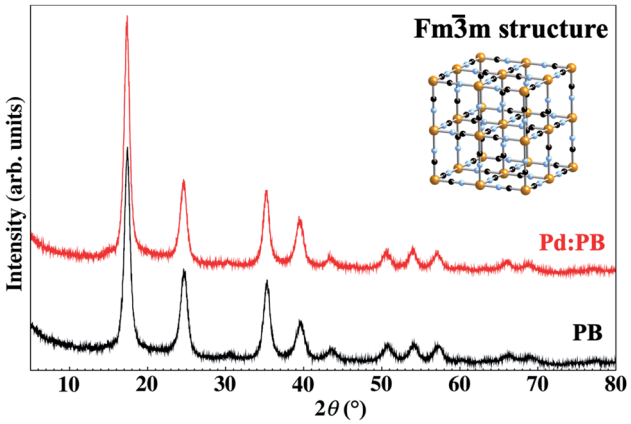

Fig. 7 Powder XRD patterns of the pristine (black) and Pd-sorbed (red) PBs. The crystal structure of PB is shown in the inset.

almost the same as for each other, it is reasonably concluded that the Pd^{2+} ion substitution with Fe^{2+} ion proceeded with the maintenance of the jungle-gym structure.

The conclusions on the uptake mechanism of Pd ions into PBNPs can allow us to estimate the substitution rate of Fe^{2+} with Pd^{2+} from the results of Table 1, by considering the PB unit cell (Fig. 1) with the inclusion of four Fe^{2+} and four Fe^{3+} atoms. Assuming that the amount of Fe(II) elution is equal to that of the Pd(II) substitution (namely, the amount of Pd and Fe diffusion inside the nanospace of PBNPs is neglected), the substitution efficiency was obtained to be 87%. This implied that 0.30 g of Pd can be recovered using 1 g of PB with a chemical form of $KFe^{III}[Fe^{II}(CN)_6]$. As shown in Table 1, if the uptake mechanism of Ru and Rh ions into PBNPs proceeds in a manner similar to that of Pd ions (substitution with Fe^{2+}/Fe^{3+}), their substitution efficiency and the amount of uptake per 1 g of PB can be predicted, as the values with asterisk (*) in Table 1. This is in progress for Ru and Rh elements.

Thus, the present findings demonstrate that PB (or its analogues) will be one of the candidates to be developed to recycle the noble and rare metals from E- and N-wastes.

4. Summary

We have examined the uptake mechanism of Pd ions to PBNPs in the nitric acid solution for the 24 h sorption test *via* HR-TEM, powder XRD, and UV-Vis-NIR spectroscopy techniques in combination with first principles calculations and revealed that the Pd^{2+} ions are sorbed into PBNPs by substitution with Fe^{2+} ions of the PB framework while maintaining the PB framework. Assuming that the amount of Fe(II) elusion is equal to that of Pd(II) substitution, the substitution efficiency is estimated to be 87%. This implied that 0.30 g of Pd can be recovered using 1 g of PB. The present findings demonstrate that PB (or its analogues) will be one of the candidates to be developed to recycle the noble and rare metals from E- and N-wastes.

Conflicts of interest

There are no conflicts to declare.

Acknowledgements

The present work was financially supported by "The R&D program for advanced nuclear power systems" from MEXT (Ministry of Education, Culture, Sports, Science and Technology), and partly by Chubu Electric Power Co. Ltd. The CASTEP calculations were performed by using "Computer System for Nanostructure Design" of Venture Business Laboratory, Nagoya University.

References

1 G. B. Haxel, J. B. Hedrick and G. J. Orris, *Rare Earth Elements: Critical Resources for High Technology*, USGS Fact Sheet, 087-02, 2002.
2 H. Asano and M. Aritomi, Long-Term Integrity of Waste Package Final Closure for HLW Geological Disposal, (I) Points at Issue Concerning 1,000 Years Containment Capability of Overpack, *J. Nucl. Sci. Technol.*, 2005, **42**, 470–479.
3 O. Tochiyama and S. Masuda, Building technical and social confidence in the safety of geological disposal in Japan, *J. Nucl. Sci. Technol.*, 2013, **50**, 665–673.
4 A. H. Gallardo, T. Matsuzaki and H. Aoki, Geological storage of nuclear wastes: insights following the Fukushima crisis, *Energy Policy*, 2014, **73**, 391–400.
5 T. Inoue, M. Sakata, H. Miyashiro, T. Matsumura, A. Sasahara and N. Yoshiki, Development of partitioning and transmutation technology for long-lived nuclides, *Nucl. Technol.*, 1991, **93**, 206–220.
6 K. Uruga, K. Sawada, Y. Arita, Y. Enokida and I. Yamamoto, Removal of Platinum Group Metals Contained in Molten Glass Using Copper, *J. Nucl. Sci. Technol.*, 2007, **44**, 1024–1031.
7 R. Mishima, Y. Inaba, S. Tachioka, M. Harigai, S. Watanabe, J. Onoe, M. Nakase, T. Matsumura and K. Takeshita, Sorption properties of aluminum hexacyanoferrate for platinum group elements, *Chem. Lett.*, 2020, **49**, 83–86.
8 K. Takeshita, Y. Inaba, T. Takahashi, J. Onoe and H. Narita, Development of separation process of PGMs and Mo from high-level liquid waste for the stable operation of vitrification process, *Proceedings of Global 2015*, 2015, pp. 20–24.
9 T. Onishi, K. Sekioka, M. Suto, K. Tanaka, S. Koyama, Y. Inaba, H. Takahashi, M. Harigai and K. Takeshita, Adsorption of platinum-group metals and molybdenum onto aluminum ferrocyanide in spent fuel solution, *Energy Procedia*, 2017, **131**, 151–156.
10 S. Kitagawa, R. Kitaura and S. Noro, Functional Porous Coordination Polymers, *Angew. Chem., Int. Ed.*, 2004, **43**, 2334–2375.
11 Z. Chang, D. Yang, J. Xu, T. Hu and X. Bu, Flexible Metal–Organic Frameworks: Recent Advances and Potential Applications, *Adv. Mater.*, 2015, **27**, 5432–5441.
12 K. K. Gangu, S. Maddila, S. B. Mukkamala and S. B. Jonnalagadda, A review on contemporary metal–

organic framework materials, *Inorg. Chim. Acta*, 2016, **446**, 61–74.

13 A. Gotoh, H. Uchida, M. Ishizaki, T. Satoh, S. Kaga, S. Okamoto, M. Ohta, M. Sakamoto, T. Kawamoto, H. Tanaka, M. Tokumoto, S. Hara, H. Shiozaki, M. Yamada, M. Miyake and M. Kurihara, *Nanotechnology*, 2007, **18**, 345609.

14 T. Yamamoto, N. Saso, Y. Umemura and Y. Einaga, Photoreduction of Prussian Blue Intercalated into Titania Nanosheet Ultrathin Films, *J. Am. Chem. Soc.*, 2009, **131**, 13196–13197.

15 D. S. Middlemiss, D. Portinari, C. P. Grey, C. A. Morrison and C. C. Wilson, Spin crossover in the CsFeII[CrIII(CN)6] Prussian blue analog: phonons and thermodynamics from hybrid functionals, *Phys. Rev. B: Condens. Matter Mater. Phys.*, 2010, **81**, 184410.

16 H. Tokoro and S. Ohkoshi, Multifunctional Material: Bistable Metal-Cyanide Polymer of Rubidium Manganese Hexacyanoferrate, *Bull. Chem. Soc. Jpn.*, 2015, **88**, 227–239.

17 W. Zhang, S. Hu, J. Yin, W. He, W. Lu, M. Ma, N. Gu and Y. Zhang, Prussian Blue Nanoparticles as Multienzyme Mimetics and Reactive Oxygen Species Scavengers, *J. Am. Chem. Soc.*, 2016, **138**, 5860–5865.

18 X. Wu, M. Shao, C. Wu, J. Qian, Y. Gao, X. Ai and H. Yang, Low Defect FeFe(CN)6 Framework as Stable Host Material for High Performance Li-Ion Batteries, *ACS Appl. Mater. Interfaces*, 2016, **8**, 23706–23712.

19 M. Ishizaki, H. Ando, N. Yamada, K. Tsumoto, K. Ono, H. Sutoh, T. Nakamura, Y. Nakao and M. Kurihara, Redox-coupled alkali-metal ion transport mechanism in binder-free films of Prussian blue nanoparticles, *J. Mater. Chem. A*, 2019, **7**, 4777–4787.

20 H. Mimura, J. Lehto and R. Harjula, Selective Removal of Cesium from Simulated High-level Liquid Wastes by Insoluble Ferrocyanides, *J. Nucl. Sci. Technol.*, 1997, **34**, 607–609.

21 M. Arisaka, M. Watanabe, M. Ishizaki, M. Kurihara, R. Chen and H. Tanaka, Cesium adsorption ability and stability of metal hexacyanoferrates irradiated with gamma rays, *J. Radioanal. Nucl. Chem.*, 2015, **303**, 1543–1547.

22 A. K. Vipin, B. Fugetsu, I. Sakata, A. Isogai, M. Endo, M. Li and M. S. Dresselhaus, Cellulose nanofiber backboned Prussian blue nanoparticles as powerful adsorbents for the selective elimination of radioactive cesium, *Sci. Rep.*, 2016, **6**, 37009.

23 T. Ohnuki, Y. Aiba, F. Sakamoto, N. Kozai, T. Niizato and Y. Sasaki, Direct accumulation pathway of radioactive cesium to fruit bodies of edible mushroom from contaminated wood logs, *Sci. Rep.*, 2016, **6**, 29866.

24 H. Tachikawa, K. Haga and K. Yamada, Mechanism of K^+, Cs^+ ion exchange in nickel ferrocyanide: a density functional theory study, *Comput. Theor. Chem.*, 2017, **1115**, 175–178.

25 S. J. Clark, M. D. Segall, C. J. Pickard, P. J. Hasnip, M. I. J. Probert, K. Refson and M. C. Payne, *Z. Kristallogr.*, 2005, **220**, 567–570.

26 P. Hohenberg and W. Kohn, Inhomogeneous Electron Gas, *Phys. Rev.*, 1964, **136**, B864–B871.

27 W. Kohn and L. J. Sham, Self-Consistent Equations Including Exchange and Correlation Effects, *Phys. Rev.*, 1965, **140**, A1133–A1138.

28 D. Vanderbilt, Soft self-consistent pseudopotentials in a generalized eigenvalue formalism, *Phys. Rev. B: Condens. Matter Mater. Phys.*, 1990, **41**, 7892–7895.

29 J. P. Perdew, K. Burke and M. Ernzerhof, Generalized Gradient Approximation Made Simple, *Phys. Rev. Lett.*, 1996, **77**, 3865–3868.

30 H. J. Monkhorst and J. D. Pack, Special points for Brillouin-zone integrations, *Phys. Rev. B: Solid State*, 1976, **13**, 5188–5192.

31 M. Cococcioni and S. de Gironcoli, Linear response approach to the calculation of the effective interaction parameters in the LDA+U method, *Phys. Rev. B: Condens. Matter Mater. Phys.*, 2005, **71**, 035105.

32 H. Hurst, An Electron Diffraction Study of the Crystalline Structure of the Lipids in the Pupal Exuviae of Calliphora Erythrocephala, *J. Exp. Biol.*, 1950, **27**, 238–252.

33 T. Matsuda, J. Kim and Y. Moritomo, Symmetry Switch of Cobalt Ferrocyanide Framework by Alkaline Cation Exchange, *J. Am. Chem. Soc.*, 2010, **132**, 12206–12207.

34 C. Koch, PhD thesis, Arizona State University, 2002.

35 S. Watanabe, Y. Sawada, M. Nakaya, M. Yoshino, T. Nagasaki, T. Kameyama, T. Torimoto, Y. Inaba, H. Takahashi, K. Takeshita and J. Onoe, Intra- and inter-atomic optical transitions of Fe, Co, and Ni ferrocyanides studied using first-principles many-electron calculations, *J. Appl. Phys.*, 2016, **119**, 235102.

36 R. D. Shannon, Effective ionic radii and systematic studies of interatomic distances in halides and chaleogenides, *Acta Crystallogr., Sect. A: Cryst. Phys., Diffr., Theor. Gen. Crystallogr.*, 1976, **32**, 751–767.

37 P. Scherrer, Bestimmung der Größe und der inneren Struktur von Kolloidteilchen mittels Röntgenstrahlen, *Nachr. Ges. Wiss. Goettingen, Math.-Phys. Kl.*, 1918, 98–100.